Assessment of the rotational stiffness of single-riveted joints in a steel lattice girder by modal analysis

Hannah Franz, Emilie Lepretre, Sylvain Chataigner, Mario Rinke, Lamine Dieng

The version of record of this manuscript has been published and is available in the journal
Engineering structures** 298 **(2024)
https://doi.org/10.1016/j.engstruct.2023.117052

Assessment of the rotational stiffness of single-riveted joints in a steel lattice girder by modal analysis

H. Franz[a,b,*], E. Lepretre[a], S. Chataigner[a], M. Rinke[c], L. Dieng[a]

[a]*Université Gustave Eiffel, MAST-SMC, Allée des Ponts et Chaussées, Bouguenais, 44344, France*
[b]*AREP Group, 16 avenue d'Ivry, Paris, 75647, France*
[c]*University of Antwerp, Faculty of Design Sciences, Mutsaardstraat 31, Antwerpen, 2000, Belgium*

Abstract

Wrought-iron and mild-steel riveted lattice girders are common structural elements in the French metallic construction heritage of 1850-1930. Many rafters and purlins of roof structures of train sheds or market halls are made of flat and angle bars assembled with single-riveted joints. The assessment of the mechanical properties of those joints is key to sensitive and targeted retrofitting operations. Despite its influence on the buckling risk of lattice girders, the out-of-plane rotational stiffness of the joints has not been investigated yet. To fill this gap, experimental and numerical investigations based on modal analysis techniques were carried out on a riveted steel lattice girder dating from 1930. The measured natural frequencies and mode shapes were used to update a finite-element model of the girder. The results suggest that the single-riveted joints exhibit a rigid behaviour in the out-of-plane direction. When numerically varying the rotational joint stiffness, two indicators seem to be relevant, one based on the study of mode shapes, and the other one linked to the presence of additional numerical modes compared to the experimental measurements. Furthermore, a numerical study was conducted to assess the potential use of the findings to develop a modal-based damage detection method for riveted joints. With only one measurement point on each lattice web member, an indicator named ΔECOMAC, derived from the enhanced coordinate modal assurance criterion (ECOMAC) proposed in the literature, appears capable of detecting and localising one or several joints presenting a loss of stiffness. Overall, this paper shows that experimental modal analysis can be an eff cient tool for assessing single-riveted joints in old steel lattice girders.

Keywords: Steel lattice girders, Riveted joints, Rotational stiffness, Modal analysis, Damage detection

1. Introduction

Riveted lattice girders are essential representatives of wrought-iron and mild-steel structures from the 19th and beginning of the 20th century. In France, many roof structures of train sheds

*Corresponding author.
Email address: hannah.franz@univ-eiffel.fr (H. Franz)

or market halls from this period have been preserved, in which riveted lattice girders are used as purlins or rafters (see Fig. 1). They feature repetitive constructive patterns: they commonly consist in flats and angles assembled with single-riveted joints made by hot riveting. In train shed restorations of the last twenty years, riveted lattice purlins or rafters have often been reinforced because of numerically identified stability problems. The issues concerned out-of-plane buckling of either web members or the chords (see Fig. 2). In reality however, excessive deformations rarely occur. A refined assessment of the structural performance is therefore a key to sensitive and targeted retrofitting operations.

Figure 1: View of the roof structure of the railway station Gare d'Austerlitz built in 1869, under renovation in 2016, Paris, France (Picture from SNCF-AREP by M. Lee Vigneau).

The stability of trusses depending on various boundary conditions, especially the joint stiffness, is an active and wide research field [1][2][3]. Regarding out-of-plane buckling for triangulated and lattice structures, Eurocode 3 recommends, by default, to take the buckling length of chord and web members equal to the system length [4]. This corresponds to the assumption that all connections are hinged in the out-of-plane direction. However, the assessment of the lateral buckling risk

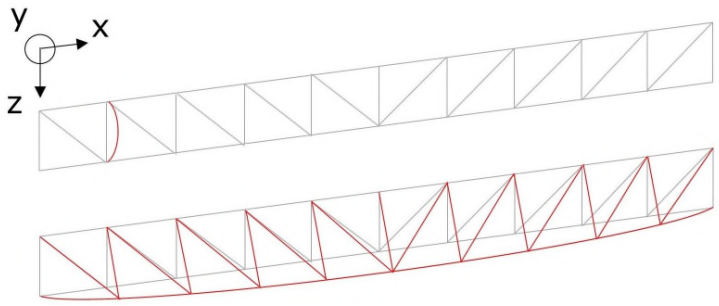

(a)

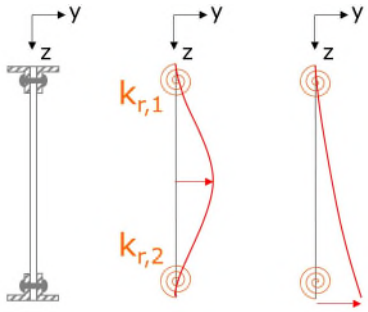

(b)

Figure 2: Common instability types identified numerically for riveted lattice girders: (a) 3D-view of a typical local buckling mode and a global buckling mode; (b) view of a typical cross-section with the deformations associated with a local buckling mode and a global buckling mode. $k_{r,1}$ and $k_{r,2}$ represent the rotational stiffness of the riveted joints.

for trusses actually depends strongly on the modelling assumptions regarding the out-of-plane rotational stiffness of the joints [5]. The end restraint provided to web members depends both on the flexural and torsional stiffness of the chords and the rotational joint stiffness at the web-to-chord location [2]. Reciprocally, the lateral restraint provided by lattice web members to one chord, given that the other chord is otherwise restrained, is activated by the joints' rigidity [1]. Assessing the rotational joint stiffness in riveted lattice girders can therefore favour a less conservative assessment of their buckling risk.

The behaviour of riveted connections is the subject of numerous studies. Hot riveting fell into

disuse, but other riveting techniques are still being investigated for applications in the transport industry [6]. In the field of structural engineering, the interest in hot-riveting is related to heritage preservation. Experimental studies regarding hot-driven rivets have mainly focused on identifying failure modes for simple splice joints and assessing the associated shear strength, in relationship with various parameters related to the material properties [7] and the geometry [8]. Some testing campaigns investigated the initial shear stiffness of lap joints [9][10]. The rotational stiffness of riveted connections has been studied only numerically, and for more complex riveted connections typical of old bridges [11][12][13]. The out-of-plane rotational stiffness of single-riveted joints typical of lattice girders has not been investigated yet.

Riveted connections made by hot riveting are sensitive to the manufacturing process. The residual tensile force in the rivets results from the driving temperature during the hot riveting process [14] and has been shown to be effectively largely scattered [15]. A low clamping force can be responsible for interfacial corrosion between the joined plates, called pack rust [7], or relative sliding. It can therefore be of interest to detect rivets providing an insuff ciently tight connection by measuring the rotational joint stiffness. As the variability of clamping forces has an effect on mechanical properties of riveted joints such as the slip resistance [8] and the fatigue strength [15], the rotational stiffness of riveted joints may also be used as an indicator of the clamping force.

This paper aims to assess the out-of-plane rotational stiffness of single-riveted joints in iron and steel lattice girders, in order to improve the buckling risk assessment on the one hand, and to detect loose connections on the other hand. The chosen investigation method relies on experimental and numerical modal analysis. This non-destructive approach has already proven useful for the identification of the rotational stiffness of joints in existing truss structures [16][17]. The

experimental modal analysis presented in this paper was carried out on a riveted lattice girder dating from 1930 collected from a demolition site. A finite element model of the girder was generated with Hexagon MARC software [18]. Chords and web members were modelled using beam elements and the rotational joint stiffness was controlled by rotational springs at the connection locations. The paper first explores which outputs of the modal analysis are best suited to assess the average rotational stiffness of all single-riveted joints, by comparing the experimental results with the numerical model. A numerical study is then conducted to find a modal-based indicator capable of detecting and localising one or several joints presenting a loss of stiffness. Based on the results, some suggestions are made regarding a damage detection procedure.

2. Experimental modal analysis

2.1. Test specimen

The studied riveted metallic lattice girder specimen was collected from a demolition site. It belonged to the roof structure of platform sheds, built in 1930 at the railway station Gare de l'Est in Paris, from which a small part was dismantled in 2021 (see Fig. 3). It is a 3300 mm long Pratt-type cantilever, with a height varying from 190 mm at its tip to 340 mm at the support (see Fig. 4). The bar sections were taken from original plans and verified by measurements with a calliper. The chords are made of double L45x45x5 angles, while the web members are made of 40x7 flats. The diagonal and vertical web members are connected to the chords by single rivets of 12 mm diameter. The girder is made of mild steel. Visual inspection revealed neither apparent defects in the joints nor damage to the material.

(a)

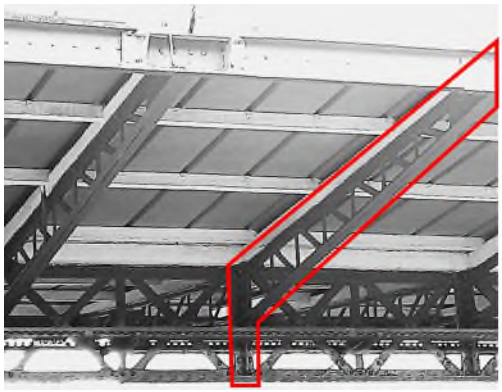

(b)

Figure 3: Original setting of the studied lattice girder: the platform sheds of the railway station Gare de l'Est built in 1930, Paris, France (Picture from SNCF-AREP).

2.2. Experimental setup

The original support conditions of the cantilever were reproduced in the laboratory. The structure was excited using an impulse hammer with a mass of 0.32 kg and an extra soft tip, resulting in a frequency range of 150 Hz. To retrieve the structure's response, 12 capacitive accelerometers, 7 single-axis and 5 tri-axis were used. Their sensitivities ranged from 100 to 1000 mV/g and their frequency bandwidth was at least 0-100 Hz. They were fixed to the girder with magnets glued on 3D-printed plastic supports, designed to fit the accelerometers (see Fig. 5).

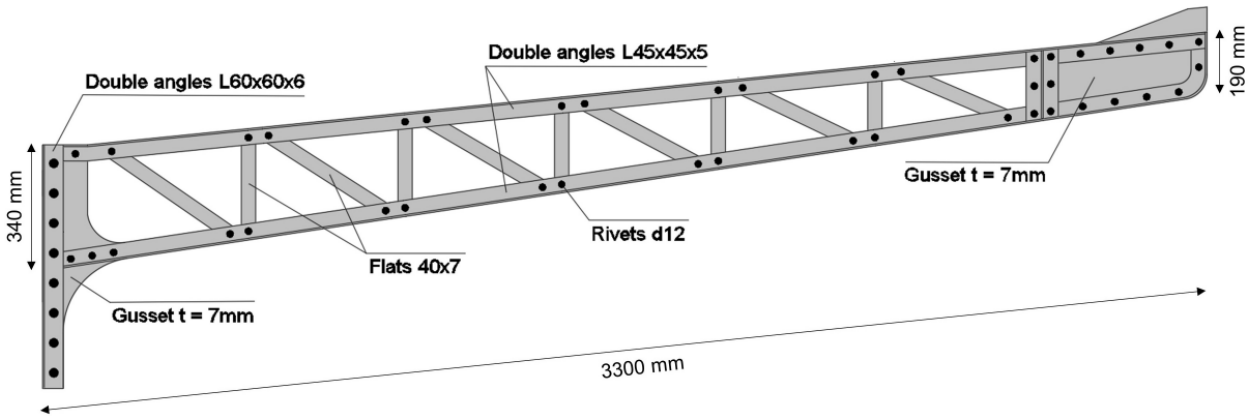

Figure 4: Elevation drawing of the tested lattice girder specimen.

To obtain satisfactory mode shapes, 30 measurement points were defined, 11 on the top chord, 11 on the bottom chord and 8 on distinct web members. Measurements of modal displacements were carried out only in the out-of-plane direction. Three sensor setups were tested (see Fig. 6):

1. A "top chord" (TC) setup with 11 accelerometers on the top chord and 1 accelerometer on the bottom chord.
2. A "bottom chord" (BC) setup with 11 accelerometers on the bottom chord and 1 accelerometer on the top chord.
3. A "web members" (WEB) setup with 8 web members equipped with 1 accelerometer at mid-length and 4 accelerometers on the top and bottom chords. The accelerometers located on diagonals were the single-axis ones, because their weight was lower than the tri-axis ones. Thus their weight remained below 10% of the weight of each web member, which is the rule-of-thumb usually recommended in practice to avoid mass loading effects.

The two accelerometers at points 11 and 14 were present in all setups, to be used as references. In each setup, the same test was repeated 7 times in order to get accurate results. The beam was excited with one horizontal impulse at the tip of the top chord. The signals were recorded with

Figure 5: View of the instrumented girder in the laboratory.

a frequency of acquisition of 4800 Hz during 2.5 seconds. After this time, out-of-plane accelerations decayed to near zero. The resulting sampling resolution was 0.4 Hz. Data acquisition was performed with the HBM Quantum X system, with a module MX1615B and a module MX1601B, and the associated software catman [19].

2.3. Digital signal processing

For each test, the excitation and response signals were transformed from the time domain to the frequency domain using Fast Fourier Transformation (FFT). The power spectral density S_{ff} of the excitation and the cross-spectral density of excitation and response S_{xf} were then computed as a multiplication of Fourier transform and Fourier transform conjugates:

$$S_{ff}(\omega) = F(\omega).F^*(\omega) \tag{1}$$

$$S_{xf}(\omega) = X(\omega).F^*(\omega) \tag{2}$$

Where F(ω) and X(ω) are the FFT transforms of the excitation (input) and the response signal (output) respectively. As each test was repeated 7 times, the spectral densities were averaged out.

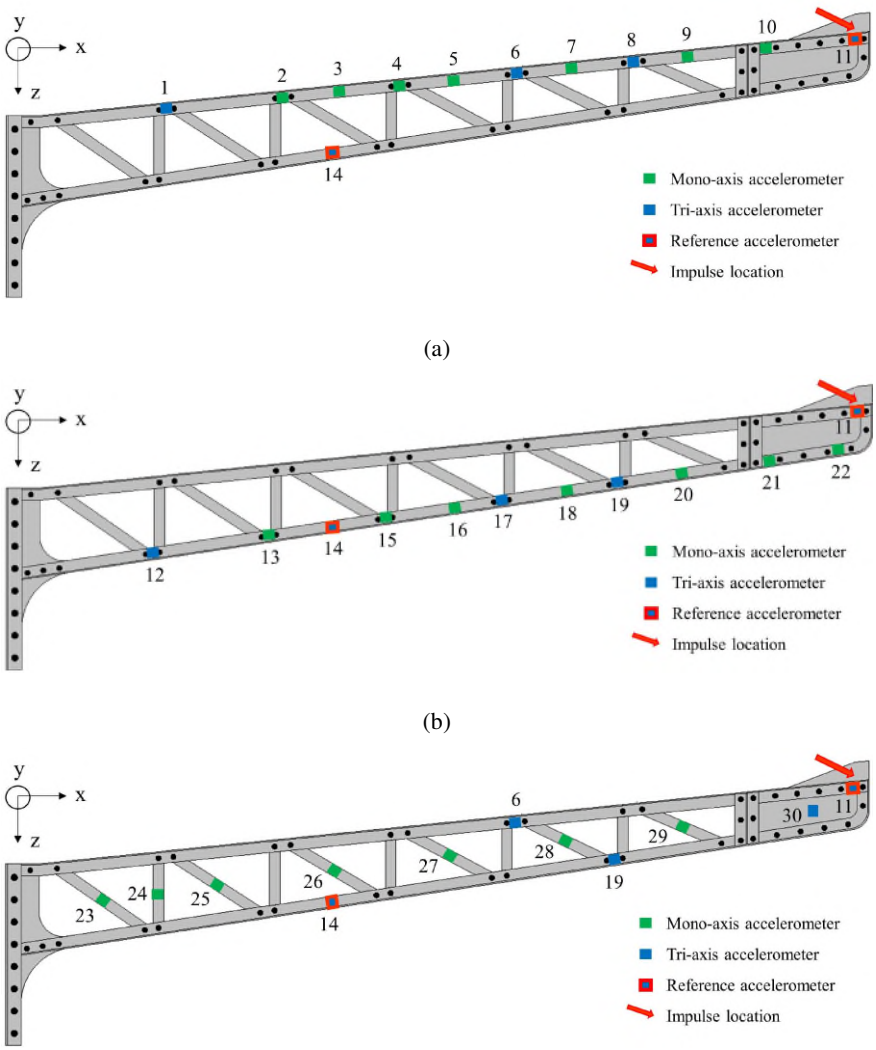

Figure 6: Sensor setups: (a) TC setup; (b) BC setup; (c) WEB setup.

They were then used to calculate an estimator of the frequency response function (FRF):

$$H(\omega) = \frac{S_{xf}}{S_{ff}} \tag{3}$$

Modal parameters were extracted using the "line-fit" method [20], through an adapted existing Matlab code [21]. This single-degree of freedom "SDOF" method, performing a curve-fitting procedure for a single mode at a time, could be used instead of a more complex global method

because the modes were suff ciently distinct.

3. Finite element modelling

3.1. Finite elements

The finite element model was built with Hexagon MARC software (see Fig. 7). The chords and web members were modelled using beam elements. Originally, all beam elements were 2-node elastic straight Bernoulli elements with cubic normal displacement interpolation (type 52 from MARC's element library [22])). The chords and web members fulfilled the Bernoulli conditions in terms of aspect ratio in the out-of-plane direction (i.e. length-to-thickness ratio above 10). The assumption behind this verification was that the reference length for the chords corresponded to the wavelength of the highest studied mode, which was about 3.1 m. When the beam elements were modelled using type 52, the torsional stiffness factor, corresponding to the St Venant torsional constant, had to be entered manually and was computed for each section with the formulas for thin-walled open sections and solid rectangles ([23]). However, the numerical results were not in satisfactory agreement with the experimental results. So the chords were modelled instead with 2-node straight thin-walled elements with linear interpolation including warping as an additional degree of freedom at each node (type 79 from MARC's element library). The web members remained with type 52 elements as warping is negligible for solid sections.

The gussets at both ends and the vertical angles at the support were modelled with triangular 3-node shell elements (type 138 from MARC's element library). The short vertical angles connecting the end gusset to the rest of the girder were modelled together as Timoshenko beam elements (type 98 from MARC's element library).

The average element size was 10 mm. As a result, the model contained 9446 elements and 5489 nodes. The chosen mesh size ensured suff cient accuracy while providing computation eff ciency. The cpu time to compute the first 10 modes was inferior to 5 seconds.

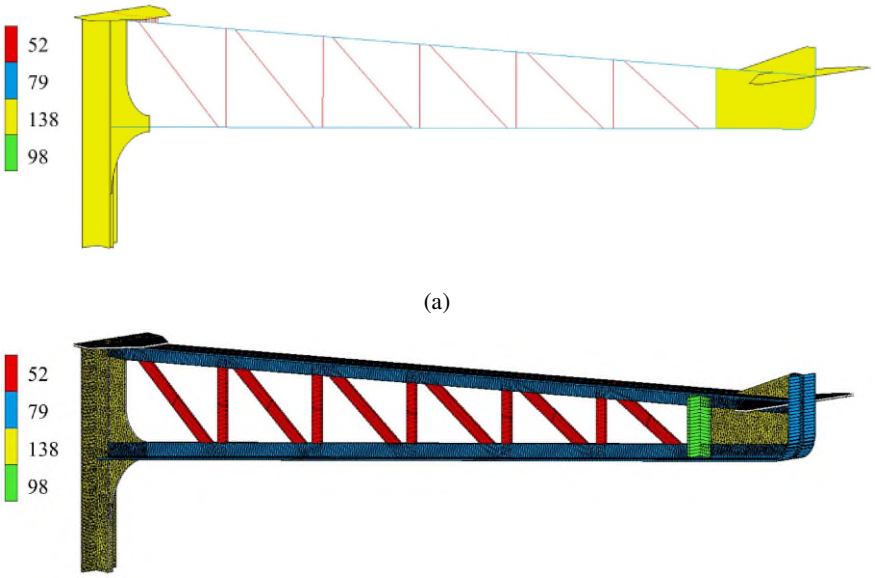

Figure 7: View of the finite element model, with associated element types. (a) outline display style; (b) expanded display style.

3.2. Material properties

The girder was made of mild steel. The elastic modulus was taken equal to 200 GPa [24] and the Poisson's ratio equal to 0.3. The volumic mass of the structure was supposed to be about 7850 kg/m^3, in line with the recommendations of the current Eurocodes for the self-weight of steel [25]. To take into account the weight of the rivets, the accelerometers and the 1 mm-thick layer of paint, an estimated equivalent volumic mass of 8450 kg/m^3 was implemented. The influence of the uncertainty regarding material properties on the modal behaviour is discussed in Sec. 4.1.

3.3. Boundary conditions

At the cantilever support, the displacements of the surfaces of the vertical angles facing the wall were fixed, probably resulting in a more rigid support condition than in reality. At the connection between chords and web members, two distinct nodes were preserved. Local coordinate systems were defined at each connection, with the z-axis going along the web member, and the x-axis pointing in the out-of-plane direction (see Fig. 8). The connecting nodes were tied for all degrees of freedom (DOF) except for DOF 5 corresponding to the out-of-plane rotation. For DOF 5, the connection was modelled with a spring of varying stiffness k_r. To model the extreme case of a hinged connection ($k_r = 0$), the connecting nodes were left independent from each other for this DOF, with no coupling condition. To model the other extreme case of a perfectly rigid connection ($k_r = \infty$), the nodes were tied for this DOF.

4. Results and discussion

The finite element model presented in section 3 takes the rotational stiffness of riveted joints as an input parameter. The modal properties of this model will now be compared to the experimental results. First, the same rotational stiffness will be attributed to all riveted joints in order to estimate which average value of the rotational stiffness yields the best agreement with the experiments and which modal-based indicators are the most useful for this purpose. Then, the rotational stiffness will be locally modified for some joints, in order to develop a modal-based indicator for damage detection.

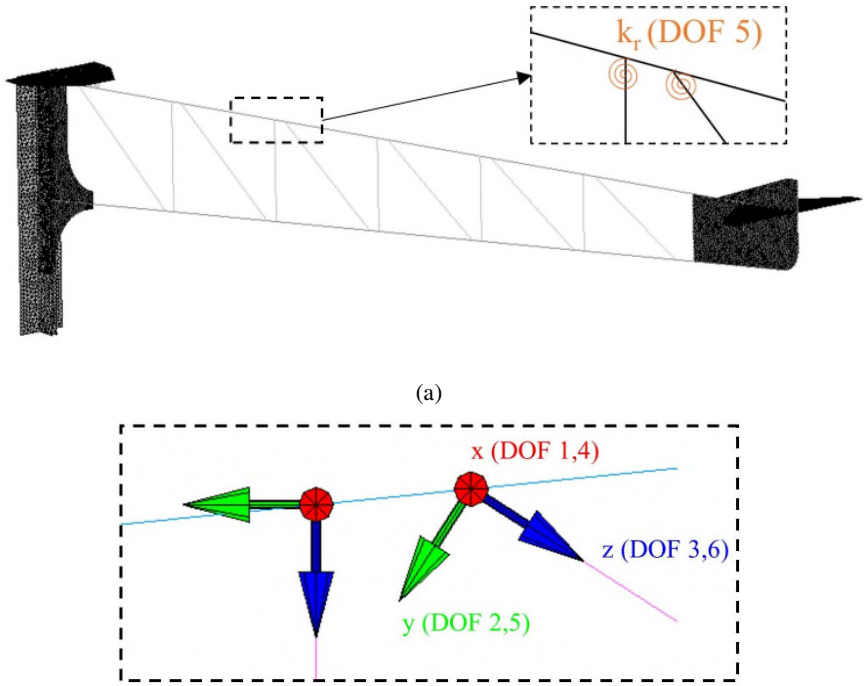

Figure 8: (a) Connections modelled with rotational springs for DOF 5; (b) Detail of local coordinate systems at the connections.

4.1. Comparison of experimental results with a numerical reference model

Experimental modal parameters were extracted for the first six modes observed on the FRFs, with frequencies below 100 Hz (see Fig. 9). Those experimental results were first compared with the modal properties of a numerical reference model. The reference model was chosen to be the model with perfect rigid connections, that is where connection nodes are tied for all 6 degrees of freedom. In the frequency range of interest, the reference model yielded 7 modes: 6 out-of-plane modes that could be fairly paired with the ones identified experimentally, and 1 in-plane mode, that could not be accounted for with the presented experimental setups. Table 1 displays the average values of the frequencies measured for the 6 modes identified experimentally and the frequencies

of the corresponding numerical modes. The numerical frequencies are up to 10% higher than the experimental ones, as expected for this model with conservative stiff boundary conditions at the cantilever support. Table 1 also presents the standard deviations that were obtained from the measured eigenfrequencies for each accelerometer in all three setups, which amount to 36 measurements in total. The frequencies were measured with a precision below 5%. Regarding uncertainties from the numerical model, it was admitted that the uncertainty on the elastic modulus was situated in the range 190-210 GPa, while the uncertainty on the volumic mass was estimated between 8300 and 8600 kg/m^3. The resulting uncertainty on the numerical frequency of each mode is a constant 3.4% compared to the reference model. Regarding the mode shapes, the considered variation of material properties had no influence.

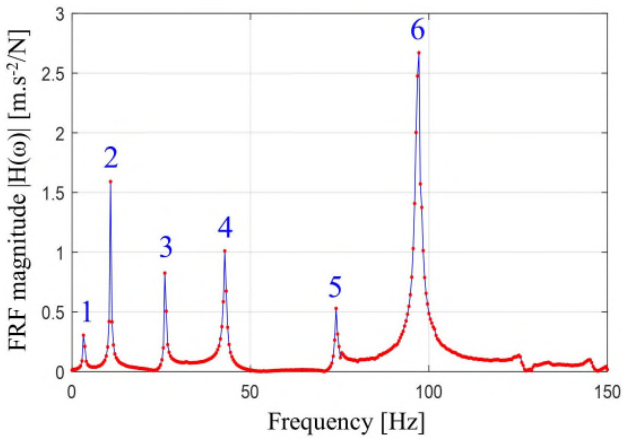

Figure 9: Inertance magnitude at point 17 in the BC setup.

Fig. 10 presents a comparison of numerical and experimental eigenfrequencies and mode shapes, for the six first out-of-plane modes. The plotted mode shapes are equivalent to a top view of the deformed structure, as only out-of-plane dis-placements along the global horizontal axis x are presented. Mode shapes were normalised following this procedure:

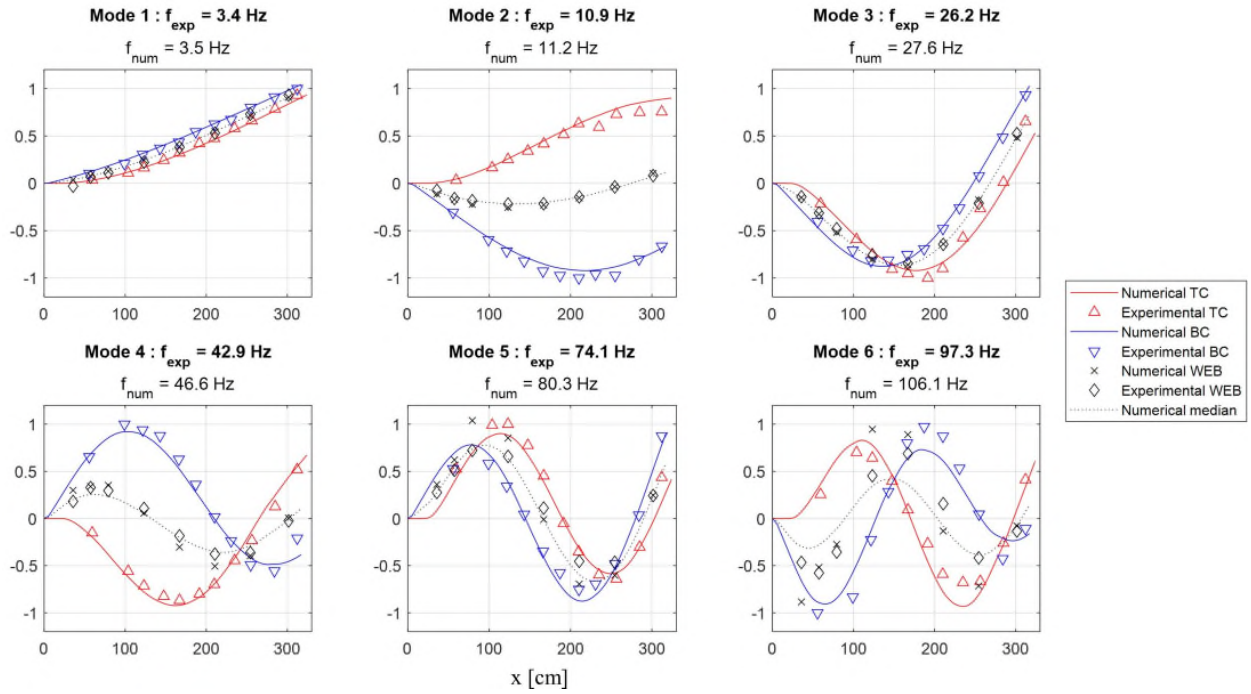

Figure 10: Comparison of numerical and experimental mode shapes (out-of-plane displacements plotted along global horizontal axis).

Experimental mode number	**EXP** f (SD) [Hz]	**NUM (ref)** f [Hz]
1	3.37 (0.12)	3.49
2	10.88 (0.37)	11.21
		24.81
3	26.17 (0.10)	27.60
4	42.92 (0.06)	46.62
5	74.09 (0.20)	80.35
6	97.29 (0.24)	106.15

*grey: in-plane mode

Table 1: Experimental frequencies, with their standard deviation (sd), and corresponding numerical frequencies obtained with the reference model.

1. The experimental mode shapes were first re-scaled so that the maximum amplitude of the top or the bottom chord was equal to 1.

2. The numerical mode shapes were then re-scaled so as to obtain the best fit between the numerical and experimental mode shapes of the chords (least-square method).

The mode shapes were found to be in very good agreement for the first four modes. Real discrepancies appeared for modes 5 and 6. In Fig. 10, the numerical median between top and bottom chords' displacements is plotted as a dotted line. It enhances that in mode 5, the numerical mode shape exhibited large web member deformations, while in the experimental mode shape, web member deformations remained closer to the median. Fig. 11 provides a visualization of the numerical mode shape of the 5^{th} out-of-plane mode. In mode 6, the fitting between experimental and numerical mode shapes is overall less satisfactory.

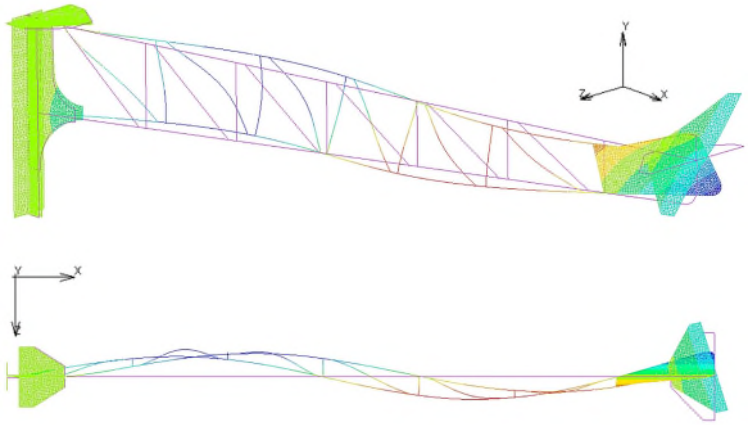

Figure 11: 3d-view and top view of the deformed and original states of the structure for the 5^{th} mode, obtained with the numerical reference model (fully rigid connections). The colours correspond to different quantities of out-of-plane displacements along z-axis.

This section presented the tools used to compare the finite element model with the experimental results. The comparison was first made for a numerical reference model in order to validate the modelling assumptions presented in section 3. In this reference model, the riveted joints were modelled with tied nodes, which corresponds to perfectly rigid connections ($k_r = \infty$). Now differ-

ent values of rotational stiffness k_r will be implemented.

4.2. Assessment of the average rotational stiffness of the riveted joints

In order to assess the average rotational stiffness of the riveted joints, a parametric study was conducted. The outputs of the numerical modal analysis for different input values of the rotational joint stiffness k_r were compared to the experimental results as for the reference model, to identify which stiffness k_r yielded the best agreement with the measurements. The same stiffness k_r was attributed to all riveted joints.

The range of studied stiffness values was defined based on the stiffness indice R [26]:

$$R = k_r \frac{L}{EI} \tag{4}$$

Where L and EI are the length and the rigidity of the web member connected to the riveted joint of interest. In the case of a hinged connection, R is equal to 0, while in the case of a rigid connection R is tending towards the infinity. To model a near-hinged connection, R must be small, while to model a near-rigid connection, R must be large. Stiffness values were therefore chosen so that R varied approximately between 0.01 and 100. The same rotational stiffness k_r was assigned to all connections, even though web members had varying lengths. As a consequence, to obtain roughly $R = 0.01$ and $R = 100$ for all the web members, k_r was taken equal to 10^4 N.mm/rad and 10^8 N.mm/rad respectively. $k_r = 10^6$ N.mm/rad was tested as an intermediary case. It is acknowledged that the same joint stiffness does not offer the same degree of restraint to all web members.

Table 2 presents the obtained frequencies for different values of joint stiffness. The maximum considered frequency was chosen as the frequency of the 6^{th} out-of-plane mode of the reference

model (f=106.15 Hz). As reducing k_r from the infinite (perfectly "rigid" connection) to zero (perfectly "hinged" connection) decreased the overall rigidity of the structure, the expected frequencies corresponding to the experimental modes had to be lower than 106.15 Hz.

Considering the frequencies of the first five out-of-plane modes, it seems from Table 2 that the model with hinged connections provides a better agreement with the measured frequencies presented in Table 1. However, it must be reminded that the support conditions of the numerical model were stiffer than reality, potentially yielding higher frequencies. The frequencies of the first modes are therefore not considered as a reliable indicator in this study. Indicators other than the frequencies need to be be proposed.

Table 2 highlights one important effect of lowering the out-of-plane rotational joint stiffness: in the models with lower stiffness k_r, a number of additional modes appeared. Those modes were dominated by the deformations of one or several web members. Despite measurement points being located on web members in the WEB setup, those modes were not observed experimentally. The horizontal dashed line in Table 2 shows the limit above which it was not possible to attribute numerical modes to experimental ones. For example, in the model with $k_r = 10^6$ N.mm/rad, the modes 7 and 8 had close frequencies and mode shapes, and they were not in satisfactory agreement with the experimental 6^{th} mode. Thus the presence or absence of additional modes compared to the modes identified experimentally is an indicator suggesting that the models with higher stiffness k_r are in better agreement with the experiments.

Moreover, the numerical and experimental mode shapes of the six first out-of-plane modes were quantitatively compared through a quality criteria L_r proposed in [17]. For each mode r, this quantity measures the gap between the numerical and the experimental mode shapes, based on the

Numerical mode number	k_r [N.mm/rad]				
	∞ (rigid)	1,00E+08	1,00E+06	1,00E+04	0 (hinged)
1	3.49	3.49	3.46	3.42	3.41
2	11.21	11.21	11.08	10.99	10.99
3	24.81	25.05	25.03	25.01	25.00
4	27.60	27.59	27.44	27.22	27.21
5	46.62	46.60	45.93	44.38	44.31
6	80.35	80.32	78.72	74.23	73.99
7	106.15	106.07	97.50	79.85	79.60
8			104.72	85.96	85.11
9				87.06	87.14
10				93.89	93.64
11				95.57	95.29
12				105.82	105.50

*grey: in-plane mode

Table 2: Eigenfrequencies of the numerical modes in the frequency range [0-106.15] Hz.

MAC matrix ("Modal Assurance Criterion") [17]:

$$L_r = 1 - \mathrm{MAC}_r = 1 - \frac{|\phi^H_{r,\mathrm{num}}.\phi_{r,\mathrm{exp}}|^2}{\phi^H_{r,\mathrm{num}}.\phi_{r,\mathrm{num}} \cdot \phi^H_{r,\mathrm{exp}}.\phi_{r,\mathrm{exp}}} \tag{5}$$

Where ϕ_r is the eigenvector containing the mode shape deformations of mode r at the 30 measurement points of the three combined experimental setups. The exponent H indicates a horizontal vector. MAC_r is the sum of the diagonal elements of the MAC matrix. The "num" and "exp" subscripts correspond to the values obtained numerically and experimentally. L_r varies between 0 and 1. The closest L_r is to 0, the better the agreement between experimental and numerical mode shapes is.

Table 3 presents the values calculated for L_r. Those values decrease when the stiffness increases. L_r is then another indicator suggesting that the model with rigid connections best represents the experiments. The increase of L_r when k_r decreases was mostly effected due to larger web deformations in the numerical model. As an example, the numerical mode shape of mode 5

obtained with the "hinged" model is presented in Fig. 12. From the comparison with Fig. 11, it is conspicuous that the web deformations become out-of-proportion.

Experimental mode number	k_r [N.mm/rad]				
	∞ (rigid)	1,00E+08	1,00E+06	1,00E+04	0 (hinged)
1	0.20%	0.20%	0.25%	0.32%	0.32%
2	0.83%	0.83%	0.95%	1.07%	1.07%
3	1.50%	1.51%	1.72%	2.36%	2.39%
4	2.12%	2.13%	3.22%	5.01%	5.07%
5	5.23%	5.33%	14.19%	44.87%	45.36%
6	13.1%	13.53%			

Table 3: Quality criteria L_r comparing numerical and experimental mode shapes for different values of k_r.

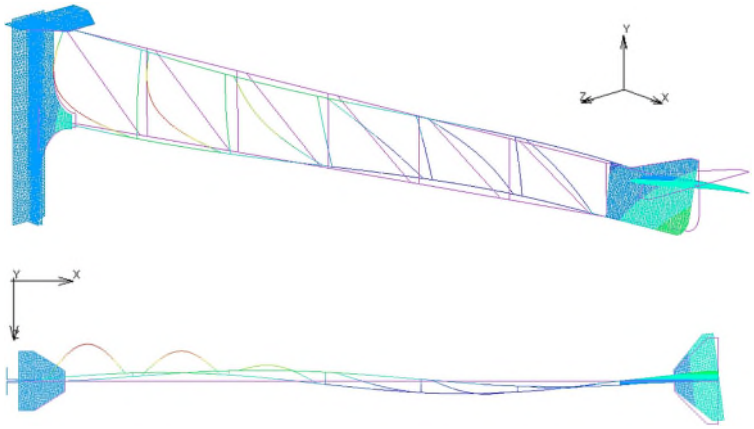

Figure 12: 3d-view and top view of the deformed and original states of the structure for the 5th mode, obtained with the "hinged" numerical model. The colours correspond to different quantities of out-of-plane displacements along the z-axis.

In this section, it was shown that attributing a lower rotational stiffness k_r to the riveted joints of the lattice girder yielded a less good agreement between numerical and experimental results than with the numerical reference model with perfect rigid joints. Two indicators were proposed to lead to this conclusion. The first indicator is the presence or absence of additional numerical modes, dominated by the vibration of web members. The second indicator is more quantitative and relies

on the quality criteria L_r, derived from the MAC matrix, measuring the gap between numerical and experimental mode shapes.

4.3. Detection of a faulty riveted joint

In section 4.2, it was assumed that the structure was healthy and that all riveted joints had the same rotational stiffness. However, in reality, the level of pre-stress is likely to vary amongst the rivets, either because of initial variations during riveting operations or because of ageing, as was mentioned in the introduction. Different clamping forces probably induce variations of the rotational stiffness amongst riveted joints. An investigation was therefore carried out to predict whether a defective riveted joint, presenting a lower rotational stiffness than the other joints of a lattice girder, could be detected by modal analysis and to determine which modal-based indicator could be used. For this purpose, damages were numerically introduced into the finite element model of the structure, by locally attributing a lower stiffness to some riveted joints. Only single-damaged models were analysed, in which only one riveted joint was released. Three specific cases were tested, corresponding to introducing damages at three selected riveted joints located at the end of vertical or diagonal web members, close or far from the cantilever support (see Fig. 13).

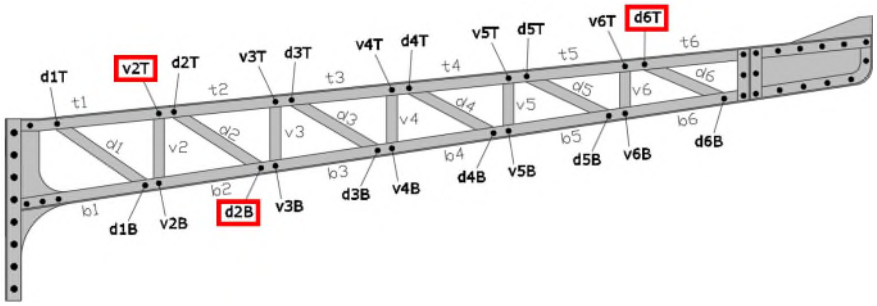

Figure 13: Location of the riveted joints that were numerically faulty.

4.3.1. Need for a refined indicator

First, single-damaged models were built, in which one riveted joint (v2T, d2B or d6T) was modelled as a hinged connection ($k_r = 0$) while all other riveted joints were modelled as rigid connections. No significant change compared to the reference model could be observed with the indicators used in section 4.2. The computed modes stayed the same, with similar frequencies and mode shapes. No additional mode appeared (see Tab. 4). The quality criteria L_r did not vary significantly either (see Tab. 5).

Numerical mode number	REF (ND)	SD (v2T - kr=0)	SD (d2B - kr=0)	SD (v6T - kr=0)
1	3.49	3.49	3.49	3.49
2	11.21	11.21	11.21	11.21
3	24.81	25.04	25.05	25.05
4	27.60	27.55	27.60	27.60
5	46.62	46.62	46.61	46.61
6	80.35	80.17	80.25	80.23
7	106.15	106.06	106.10	106.20

*grey: in-plane mode

Table 4: Eigenfrequencies of the numerical modes in the frequency range [0-110] Hz obtained with the reference model (REF) with no damage (ND) and single-damaged models (SD).

Experimental mode number	REF (ND)	SD (v2T - kr=0)	SD (d2B - kr=0)	SD (v6T - kr=0)
1	0.20%	0.18%	0.18%	0.18%
2	0.83%	0.83%	0.85%	0.84%
3	1.50%	1.53%	1.51%	1.53%
4	2.12%	2.14%	2.20%	2.17%
5	5.23%	4.68%	5.66%	4.08%
6	13.1%	11.86%	12.21%	11.09%

Table 5: Quality criteria L_r comparing numerical and experimental mode shapes for different single-damaged models.

L_r is a quantity indicating the global correlation of two sets of mode shapes, for one mode. It

is understandable that this quantity is little affected when only one connection exhibits a different behaviour. It was therefore necessary to find a mode-shape related parameter indicating for each individual measurement point the local variation of correlation between the experimental and numerical results, taking into account several chosen modes.

4.3.2. ECOMAC between single-damaged models and the reference model

The most classical parameter attempting to identify which measurement degrees-of-freedom contribute negatively to the correlation between two sets of mode shapes is the coordinate modal assurance criterion (COMAC)[20]. In order to avoid biases linked to the definition of modal vectors, the enhanced coordinate modal assurance criterion (ECOMAC) was developed [27]. The ECOMAC between two sets of mode shapes, typically numerical and experimental mode shapes, is defined as:

$$\text{ECOMAC[set1,set2]}(j) = \frac{\sum_{r=1}^{n} \phi_r^{\text{set1}}(j) - \phi_r^{\text{set2}}(j)}{2n} \tag{6}$$

where $\phi_r^{\text{set1}}(j)$ and $\phi_r^{\text{set2}}(j)$ are the components of the mode shape vector of mode r at measurement point j for two sets of data, and n is the number of modes taken into account.

The effectiveness of the ECOMAC was tested by comparing the mode shapes derived from the numerical reference model, where all joints are rigid, and the mode shapes derived from a single-damaged model. As an example, Fig. 14 presents the values of ECOMAC[num^{SD}, num^{ND}] obtained from the comparison of a single-damaged model (num^{SD}), where the rotational restraint was released ($k_r = 0$) at joint d2B, and the reference model with no damage (num^{ND}). Those values were computed for the components of the mode shapes corresponding to the location of measurement points in the experiments. The first four out-of-plane modes were taken into account.

A clear peak can be observed at measurement point 25, which corresponds to the sensor placed

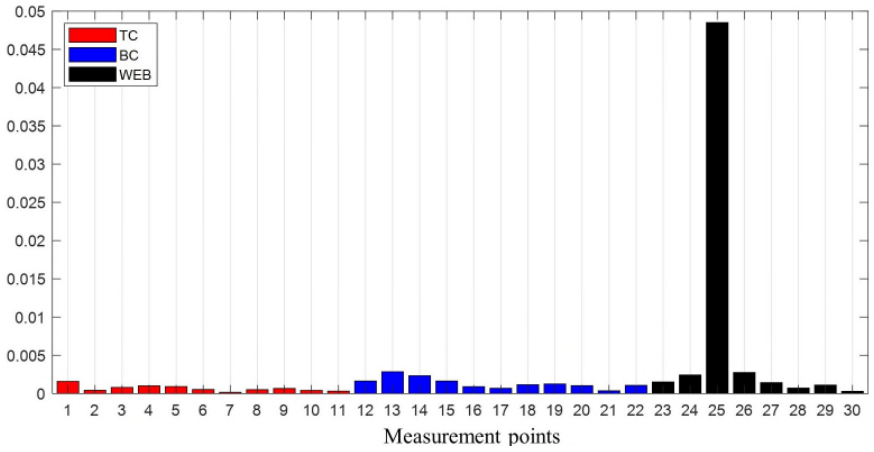

Figure 14: ECOMAC[num^{SD}, numND] (n = 6) between the single-damaged model (d2B - k_r = 0) and the reference model with all joints rigid.

on web member d2, which is connected to the bottom chord by joint d2B. Similar results are obtained when releasing the rotational restraint at v2T and d6T: peaks appear at measurement points 24 and 29 respectively. Thus it seems that the ECOMAC is capable of identifying the web member connected to a released joint. This result is in line with the common assumption used by damage detection methods relying on mode-shape related parameters, that the damage is located at the location or at the vicinity to where the change of mode shape function is the greatest [28].

4.3.3. ECOMAC between single-damaged models and the experiments

After validating that the ECOMAC could localise a damage introduced in a numerical model, the study aimed to verify whether the ECOMAC was capable of detecting a local discrepancy between the single-damaged models and the experimental results from the tested structure. Assuming the lattice girder presented in this paper is healthy, the computation of the ECOMAC between the experimental mode shapes and the numerical mode shapes derived from a single-damaged model could be expected to yield a peak as in the comparison of the single-damaged model with the

reference model. However, it is not the case. Fig. 15 presents the values of ECOMAC[num^{SD}, exp] obtained from the comparison of the single-damaged model (num^{SD}), where the rotational restraint was released ($k_r = 0$) at joint d2B, with the experiments (exp). Taking into account the first six out-of-plane modes ($n = 6$), the values of ECOMAC appear to be relatively evenly distributed over the measurement points. This is probably due to the many sources of discrepancy between the experiments and the numerical modelling, that prevail over the value attributed to the stiffness of one individual riveted joint. The ECOMAC therefore needs to be adapted.

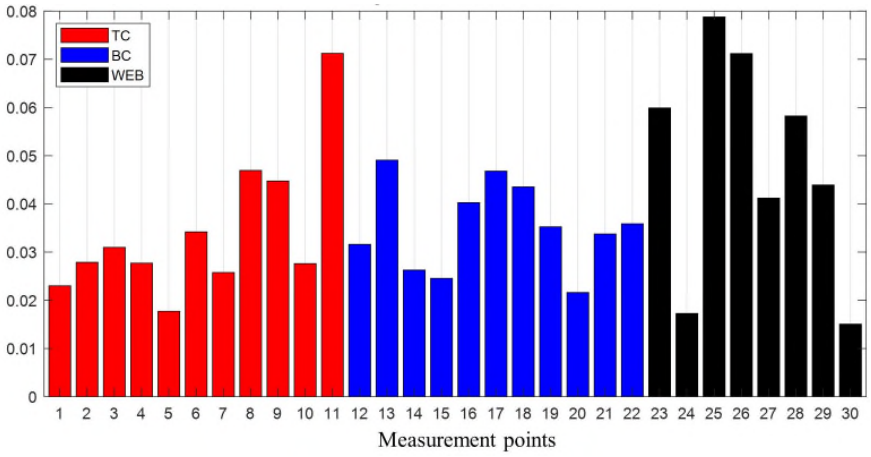

Figure 15: ECOMAC[num^{SD}, exp] ($n = 6$) between the single-damaged model (d2B - $k_r = 0$) and the experiments.

4.3.4. Introduction of ΔECOMAC

In order to filter out the "noise" created by the various sources of discrepancy other than the joint stiffness, it was decided to calculate a differential ECOMAC. This new index ΔECOMAC is the difference between the ECOMAC obtained from the comparison of the experiments and a damaged model, and the ECOMAC obtained from the comparison of the experiments and the

reference model:

$$\Delta\text{ECOMAC}[\text{num}^{\text{SD}}, \text{num}^{\text{ND}}](j) = \text{ECOMAC}[\text{num}^{\text{SD}}, \text{exp}](j) - \text{ECOMAC}[\text{num}^{\text{ND}}, \text{exp}](j) \tag{7}$$

Fig. 16 presents the differential ECOMAC between the ECOMAC[num$^{\text{SD}}$, exp] calculated for the model damaged at joint d2B ($k_r = 0$) and the ECOMAC[num$^{\text{ND}}$, exp] calculated for the reference model. A clear increase of the ECOMAC stands out at measurement point 25, corresponding to the sensor placed on diagonal d2, which is connected to the bottom chord by joint d2B. A positive peak means that locally the experimental mode shapes show a larger discrepancy with the damaged model than with the reference model, which confirms that the tested structure is healthy. It seems that the differential ECOMAC would allow to detect and localise a riveted joint with a lower rotational stiffness: the parameter ΔECOMAC is capable of identifying the web member connected to this joint, which narrows the localisation down to only two riveted joints. Again, the advantage of considering the difference of ECOMAC between the damaged model and the reference model is that it strongly reduces the discrepancies between experimental and numerical results that are not related to the joint stiffness. While many damage identification procedures rely on a well-correlated reference numerical model of the healthy structure [29], this approach allows for a larger initial discrepancy between the reference model and the experimental results. Similar results were obtained when the rotational restraint was released at joints v2T and d6T. Peaks of ΔECOMAC were then obtained at measurement points 24 and 29 respectively.

Until now, the presented ECOMAC and ΔECOMAC values took into account the first six out-of-plane modes, assuming more data would convey more information. However, computations revealed that taking into account the first four or five out-of-plane modes ($n = 4$ or $n = 5$) is

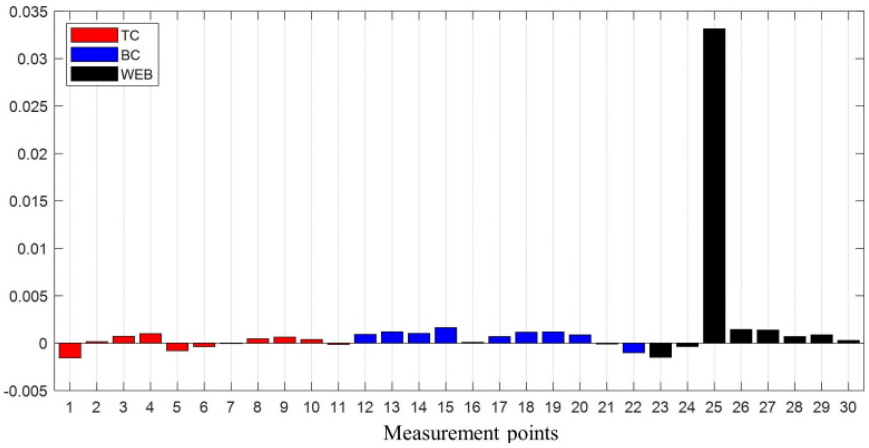

Figure 16: ΔECOMAC[num^{SD}, numND] (n = 6) for the single-damaged model (d2B - k_r = 0).

optimal to obtain unequivocal peaks. Including the sixth mode leads to less clear peaks because the reference correlation between the experiments and the reference model for this mode is not very good. Including less than four modes does not provide useable results because the rotational stiffness of riveted joints has a negligible impact on the three first modes. Taking four or five modes into account is therefore a good compromise.

4.3.5. Sensitivity of ΔECOMAC

Further simulations were conducted to evaluate the sensitivity of the criterion ΔECOMAC. The study investigated how important the loss of stiffness at a riveted joint should be to obtain a clear positive peak at the expected measurement point. It was found that peaks of ΔECOMAC were obtained even when the stiffness of a joint was very little reduced compared to the reference model. Clear peaks were observed even for a joint stiffness reduced locally to $k_r = 10^8$ N.mm/rad, which remains very close to a rigid joint. However, the absolute value of the peaks is then very small (see. Fig. 17). When the rotational stiffness is set to zero for joint d2B, the peak of ΔECOMAC at point 25 has an absolute value of about 4.1×10^{-3} for $n = 4$. When the rotational stiffness is set to

$k_r = 10^8$ N.mm/rad, then the peak has an absolute value of only 6.6×10^{-5}.

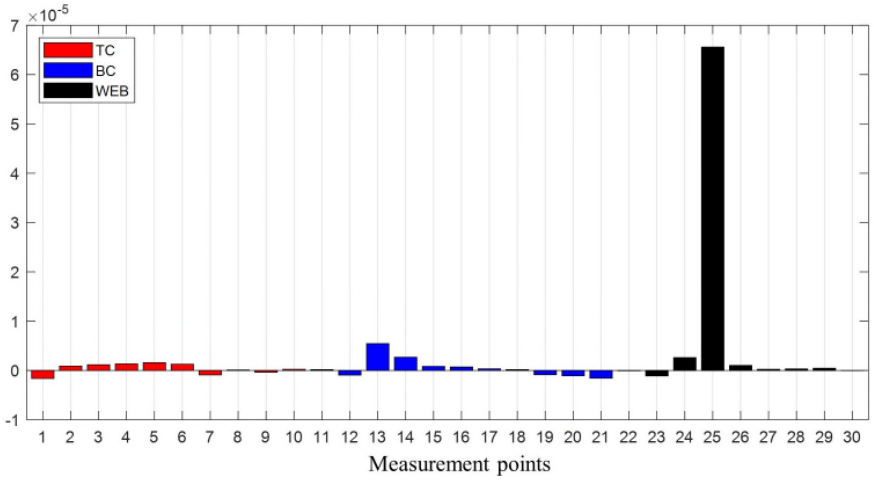

Figure 17: ΔECOMAC[num^{SD}, numND] ($n = 4$) for the single-damaged model (d2B - $k_r = 10^8$ N.mm/rad).

To establish a threshold of what a significant peak is, the absolute value of the obtained peaks was compared to the ECOMAC[num^{D}, numND] obtained at the corresponding location. The idea is that the difference between experimental and numerical results originating in a local difference of joint stiffness remains smaller than the difference between the reference model and a single-damaged model where the rotational restraint is fully released ($k_r = 0$). When a peak is obtained, it can be "normalised", yielding a ratio ζ:

$$\zeta(j) = \frac{\Delta\text{ECOMAC}[\text{num}^{SD}(k_r), \text{num}^{ND}](j)}{\text{ECOMAC}[\text{num}^{SD}(k_r = 0), \text{num}^{ND}](j)} \tag{8}$$

Fig. 18 presents the evolution of ζ for different values of reduced joint stiffness k_r. For example, when a reduced joint stiffness k_r is affected to joint d2B, peaks of ΔECOMAC are obtained at measurement point 25. $\zeta(j = 25)$ is then computed. The denominator corresponds to the ECOMAC comparing the reference model and the model with damaged joint d2B ($k_r = 0$). Let us set that a "significant" loss of stiffness corresponds to a local stiffness $k_r = 10^7$ N.mm/rad, about 10

times smaller than an almost rigid joint $k_r = 10^8$ N.mm/rad. From Fig. 18, it can be established that with $n = 4$, such a loss of stiffness can be detected by a ratio ζ of about 0.1, which means that the value of the peak of ΔECOMAC is about 10% of the ECOMAC between the reference model and the single-damaged model with $k_r = 0$.

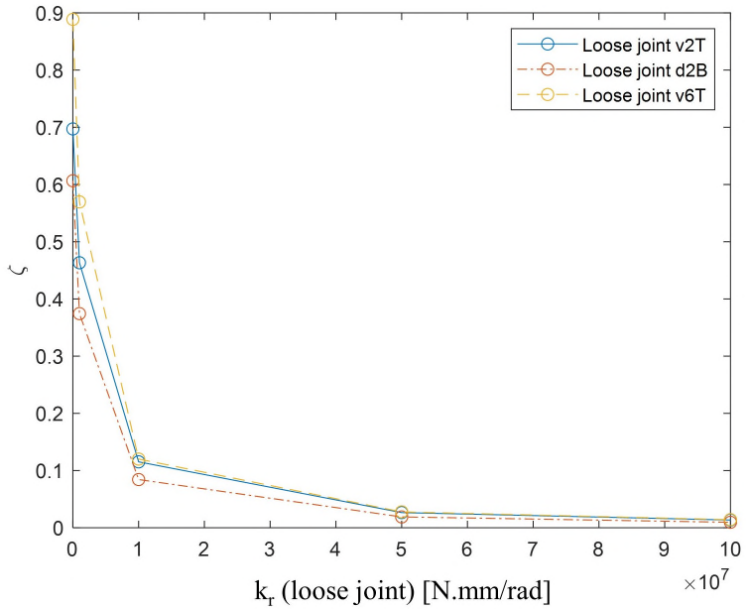

Figure 18: Ratio ζ at the peak location for different values of k_r affected to the corresponding damaged joint. Four modes were taken into account ($n = 4$).

4.3.6. Recommendations for a damage detection procedure

The investigation carried out showed that ΔECOMAC was capable of enhancing discrepancies between the healthy tested structure and numerical single-damaged models. How could ΔECOMAC be applied if damages were to be detected in an unknown potentially unhealthy riveted lattice girder? The proposed approach derived from the presented study would be:

1. to build a reference numerical model in which all riveted joints are modelled as rigid.
2. to compute ΔECOMAC for a series of single-damaged models in which the rotational re-

straint is partially released for one riveted joint of the structure. The stiffness k_r of the numerically damaged joint could correspond to $R = 10$ (instead of $R = 100$ for an almost rigid joint - see Eq. 4).

3. to detect *negative* peaks of ΔECOMAC. Indeed, if a damaged model provides locally a better agreement of numerical and experimental mode shapes than the reference model, then it would mean that the corresponding numerically damaged joint effectively exhibits a lower stiffness in reality.
4. to assess whether detected peaks are significant, by calculating the ratio ζ.

The drawback of mode-shape based methods is the necessity of having measurements from a large number of locations [29]. With the proposed approach, it becomes necessary to have only one measurement point on each diagonal. For on-site detection, the method could be implemented through a roving excitation on the diagonals, with only a few sensors located on the chords.

5. Conclusion and perspectives

This paper showed how modal analysis could be applied to assess riveted joints in old wrought-iron and mild-steel lattice girders in order to improve retrofitting operations. An experimental modal analysis was conducted on a riveted steel lattice girder and the results were confronted with modal properties obtained from a finite element model of the girder. The main conclusions are the following:

- The single-riveted joints of riveted lattice girders exhibit a rigid behaviour regarding out-of-plane rotation. The numerical reference model with rigid joints yielded a satisfactory agreement with the experiments. Decreasing the rotational joint stiffness k_r in the model

resulted in a less good agreement between numerical and experimental results. Assuming rigid riveted connections would induce a decrease of the estimated buckling risk of lattice girders based on an eigenvalue analysis. Case studies still need to be carried out to evaluate the gain of stability when modelling the riveted joints as rigid instead of hinged. This could then effectively minimise strengthening measures related to retrofitting operations.

- Two modal-based indicators were identified to obtain information on the rotational joint stiffness. The first indicator is the presence or absence of additional numerical modes, dominated by the vibration of web members. The second indicator is the gap between numerical and experimental mode shapes, due mostly to the deformations of the web members, and measured through quality criteria L_r.

- A numerical study was conducted to predict the ability of modal analysis to detect faulty riveted joints, with a lower rotational stiffness than the majority of the joints in the considered girder. The proposed indicator ΔECOMAC, comparing the agreement between the experimental mode shapes and numerical mode shapes from a reference model with rigid joints and a series of single-damaged models, seems to be able to localise the web members connected to "faulty" joints. This numerical study was predictive and requires experimental validation. A further experimental investigation is planned, in which the rivets of the tested lattice girder will progressively be replaced by bolts, with different levels of pre-stress. The impact on the modal properties will be measured using the various indicators presented in this paper. This experimental study should also help establish a relationship between the rivet clamping force and the resulting rotational joint stiffness.

Acknowledgements

This study is part of a PhD funded by AREP, subsidiary of the national French railway company SNCF (Société Nationale des Chemins de fer Français), and the French Association for Research and Technology (ANRT). The authors would like to thank the SNCF for making riveted lattice girders available for testing. They also acknowledge the support and expertise of the technicians of the SMC laboratory, who greatly contributed to setting up and carrying out the experiments.

CRediT authorship contribution statement

Hannah Franz: Conceptualization, Methodology, Software, Investigation, Writing - Original draft preparation. **Emilie Lepretre:** Methodology, Supervision, Writing - Reviewing and Editing. **Sylvain Chataigner:** Conceptualization, Supervision, Writing - Reviewing and Editing. **Mario Rinke:** Supervision, Writing- Reviewing and Editing. **Lamine Dieng:** Conceptualization, Methodology, Software, Supervision, Writing - Reviewing and Editing.

References

[1] Q.-J. Wen, Z.-X. Yue, Elastic buckling property of the upper chords in aluminum half-through truss bridges, Structures 27 (2020) 1919–1929. doi:10.1016/j.istruc.2020.07.057.

[2] S. G. Lee, R. D. Zieman, Effective length K-factors for flexural buckling strengths of web members in open web steel joists, in: Proceedings of the Annual Stability Conference, Structural Stability Research Council, Toronto, Canada, 2014.

[3] G. Somma, M. Vit, Experimental investigation of flaregroove weld stiffness in lattice girder beams by means of push-out tests, Journal of Constructional Steel Research 202 (2023). doi:10.1016/j.jcsr.2023.107780.

[4] EN 1993-1-1 Annex BB.1, Eurocode 3 : Design of steel structures - Part 1-1: General rules and rules for buildings - Annex BB.1 : Flexural buckling of members in triangulated and lattice structures, European committee for standardization (CEN), 2005.

[5] S. Timoshenko, J. Gere, Theory of elastic stability, 2nd Edition, McGraw-Hill, 1963.

[6] Y. Liao, H. Sun, G. Wu, C. Jin, J. Cui, G. Li, H. Jiang, Effect of rivet arrangement on fatigue performance of electromagneticriveted joint with 10 mm diameter rivet, International Journal of Fatigue 176 (2023). doi:10.1016/j.ijfatigue.2023.107892.

[7] Q. Collette, Riveted Connections in Historical Metal Structures (1840-1940). Hot-driven Rivets: Technology, Design and Experiments., Ph.D. thesis, Vrije Universiteit Brussel (2014).

[8] M. D'Aniello, F. Portioli, L. Fiorino, R. Landolfo, Experimental investigation on shear behaviour of riveted connections in steel structures, Engineering Structures 33 (2) (2011) 516–531. doi:10.1016/j.engstruct.2010.11.010.

[9] S. M. Jost, Behavior of Riveted Connections in Steel Truss Bridges, Master thesis, University of Washington (2012).

[10] L. Gallegos Mayorga, S. Sire, B. Plu, Experimental investigation on hot riveted double shear connections, a friction analysis, in: Structural analysis of historical constructions - Proceedings of the 10th international conference on structural analysis of historical constructions (SAHC), Leuven, Belgium, 2016.

[11] M. Al-Emrani, R. Kliger, FE analysis of stringer-to-floor-beam connections in riveted railway bridges, Journal of Constructional Steel Research 59 (7) (2003) 803–818. doi:10.1016/S0143-974X(02)00114-1.

[12] B. M. Imam, T. D. Righiniotis, M. K. Chryssanthopoulos, Numerical modelling of riveted railway bridge connections for fatigue evaluation, Engineering Structures 29 (11) (2007) 3071–3081. doi:10.1016/j.engstruct.2007.02.011.

[13] O. Minor, P. Ryjáček, Rotational Stiffness of Connections in a Historical Steel Railway Bridge, in: Structural Analysis of Historical Constructions, Springer, Cham, 2019, pp. 1082–1089.

[14] E. Leprêtre, S. Chataigner, L. Dieng, L. Gaillet, H. Cannard, Numerical and experimental investigations of hot driven riveting process on old metal structures, Engineering Structures 127 (2016) 583–593. doi:10.1016/j.engstruct.2016.08.056.

[15] D. Leonetti, J. Maljaars, G. Pasquarelli, G. Brando, Rivet clamping force of as-built hot-riveted connections in steel bridges, Journal of Constructional Steel Research 167 (Apr. 2020). doi:10.1016/j.jcsr.2020.105955.

[16] T. M. H. Luong, Identification of the state of stress in iron and steel truss structures by vibration–based experimental investigations, Ph.D. thesis, TU Cottbus-Senftenberg (2018).

[17] K. Szopa, M. Iwaniec, J. Iwaniec, Modelling and identification of bolted truss structure with the use of design of experiment approach, Structures 27 (2020) 462–473. doi:10.1016/j.istruc.2020.05.047.

[18] HEXAGON - Marc [cited 2023-07-18].
URL `https://hexagon.com/fr/products/marc`

[19] HBM - catman [cited 2023-07-18].
URL `https://www.hbm.com/fr/2290/catman-logiciel-acquisition-de-donnees/?product_type_no=Logiciel\DAQ`

[20] D. J. Ewins, Modal testing: theory, practice, and application, 2nd Edition, Research Studies Press, Baldock, Hertfordshire, England ; Philadelphia, PA, 2000.

[21] C. Hondermarck, Analyse vibratoire des câbles tendus - détermination des paramètres mécaniques de fonctionnement : tension, endommagement..., Master's thesis, Laboratoire Central des Ponts et Chaussées (2007).

[22] MARC 2018.1, Volume B: Element Library, MSC Software, 2018.

[23] A. F. Hugues, D. C. Iles, A. S. Malik, Design of steel beams in torsion, SCI, Askot, United Kingkom, 2011.

[24] K. Brandes, Eigenschaften alter Eisen und Stähle und ihre adäquate Materialprüfung und Bewertung, Bautechnik 85 (6) (2008) 394–406.

doi:10.1002/bate.200810031.

[25] EN 1991-1-1 Annex A, Eurocode 1: Actions on structures - Part 1-1: General actions - Densities, self-weight, imposed loads for buildings - Annex A, European committee for standardization (CEN), 2003.

[26] A. Palacio-Betancur, J. D. Aristizabal-Ochoa, Statics, stability and vibration of non-prismatic linear beam-columns with semirigid connections on elastic foundation, Engineering Structures 181 (2019) 89–94. doi:10.1016/j.engstruct.2018.12.002.

[27] D. L. Hunt, Application of an enhanced coordinate modal assurance criterion, in: 10th International Modal Analysis Conference, 1992, pp. 66–71.

[28] N. Maia, J. Silva, E. Almas, R. Sampaio, Damage detection in structures: from mode shape to frequency response function methods, Mechanical Systems and Signal Processing 17 (3) (2003) 489–498. doi:10.1006/mssp.2002.1506.

[29] E. P. Carden, P. Fanning, Vibration Based Condition Monitoring: A Review, Structural Health Monitoring 3 (4) (2004) 355–377. doi:10.1177/1475921704047500.